Analysis techniques for the evaluation of the neutrinoless double-β decay lifetime in ^{130}Te with the CUORE-0 detector

C. Alduino,[1] K. Alfonso,[2] D. R. Artusa,[1,3] F. T. Avignone III,[1] O. Azzolini,[4] T. I. Banks,[5,6] G. Bari,[7] J. W. Beeman,[8] F. Bellini,[9,10] A. Bersani,[11] M. Biassoni,[12,13] C. Brofferio,[12,13] C. Bucci,[3] A. Caminata,[11] L. Canonica,[3] X. G. Cao,[14] S. Capelli,[12,13] L. Cappelli,[11,3,15] L. Carbone,[13] L. Cardani,[9,10,*] P. Carniti,[12,13] N. Casali,[9,10] L. Cassina,[12,13] D. Chiesa,[12,13] N. Chott,[1] M. Clemenza,[12,13] S. Copello,[16,11] C. Cosmelli,[9,10] O. Cremonesi,[13,†] R. J. Creswick,[1] J. S. Cushman,[17] I. Dafinei,[10] A. Dally,[18] C. J. Davis,[17] S. Dell'Oro,[3,19] M. M. Deninno,[7] S. Di Domizio,[16,11] M. L. Di Vacri,[3,20] A. Drobizhev,[5,6] D. Q. Fang,[14] M. Faverzani,[12,13] G. Fernandes,[16,11] E. Ferri,[12,13] F. Ferroni,[9,10] E. Fiorini,[13,12] S. J. Freedman,[6,5,‡] B. K. Fujikawa,[6] A. Giachero,[13] L. Gironi,[12,13] A. Giuliani,[21] L. Gladstone,[22] P. Gorla,[3] C. Gotti,[12,13] T. D. Gutierrez,[23] E. E. Haller,[8,24] K. Han,[17,6] E. Hansen,[22,2] K. M. Heeger,[17] R. Hennings-Yeomans,[5,6] K. P. Hickerson,[2] H. Z. Huang,[2] R. Kadel,[25] G. Keppel,[4] Yu. G. Kolomensky,[5,25] K. E. Lim,[17] X. Liu,[2] Y. G. Ma,[14] M. Maino,[12,13] L. Marini,[16,11] M. Martinez,[9,10,26] R. H. Maruyama,[17] Y. Mei,[6] N. Moggi,[27,7] S. Morganti,[10] P. J. Mosteiro,[10] C. Nones,[28] E. B. Norman,[29,30] A. Nucciotti,[12,13] T. O'Donnell,[5,6] F. Orio,[10] J. L. Ouellet,[22,5,6] C. E. Pagliarone,[3,15] M. Pallavicini,[16,11] V. Palmieri,[4] L. Pattavina,[3] M. Pavan,[12,13] G. Pessina,[13] V. Pettinacci,[10] G. Piperno,[9,10] S. Pirro,[3] S. Pozzi,[12,13] E. Previtali,[13] C. Rosenfeld,[1] C. Rusconi,[13] E. Sala,[12,13] S. Sangiorgio,[29] D. Santone,[3,20] N. D. Scielzo,[29] V. Singh,[5] M. Sisti,[12,13] A. R. Smith,[6] L. Taffarello,[31] M. Tenconi,[21] F. Terranova,[12,13] C. Tomei,[10] S. Trentalange,[2] G. Ventura,[32,33] M. Vignati,[10] S. L. Wagaarachchi,[5,6] B. S. Wang,[29,30] H. W. Wang,[14] J. Wilson,[1] L. A. Winslow,[22] T. Wise,[17,18] A. Woodcraft,[34] L. Zanotti,[12,13] G. Q. Zhang,[14] B. X. Zhu,[2] S. Zimmermann,[35] and S. Zucchelli[36,7]

(CUORE Collaboration)

[1]*Department of Physics and Astronomy, University of South Carolina, Columbia, South Carolina 29208, USA*
[2]*Department of Physics and Astronomy, University of California, Los Angeles, California 90095, USA*
[3]*INFN - Laboratori Nazionali del Gran Sasso, Assergi (L'Aquila) I-67010, Italy*
[4]*INFN - Laboratori Nazionali di Legnaro, Legnaro (Padova) I-35020, Italy*
[5]*Department of Physics, University of California, Berkeley, California 94720, USA*
[6]*Nuclear Science Division, Lawrence Berkeley National Laboratory, Berkeley, California 94720, USA*
[7]*INFN - Sezione di Bologna, Bologna I-40127, Italy*
[8]*Materials Science Division, Lawrence Berkeley National Laboratory, Berkeley, California 94720, USA*
[9]*Dipartimento di Fisica, Sapienza Università di Roma, Roma I-00185, Italy*
[10]*INFN - Sezione di Roma, Roma I-00185, Italy*
[11]*INFN - Sezione di Genova, Genova I-16146, Italy*
[12]*Dipartimento di Fisica, Università di Milano-Bicocca, Milano I-20126, Italy*
[13]*INFN - Sezione di Milano Bicocca, Milano I-20126, Italy*
[14]*Shanghai Institute of Applied Physics, Chinese Academy of Sciences, Shanghai 201800, China*
[15]*Dipartimento di Ingegneria Civile e Meccanica, Università degli Studi di Cassino e del Lazio Meridionale, Cassino I-03043, Italy*
[16]*Dipartimento di Fisica, Università di Genova, Genova I-16146, Italy*
[17]*Department of Physics, Yale University, New Haven, Connecticut 06520, USA*
[18]*Department of Physics, University of Wisconsin, Madison, Wisconsin 53706, USA*
[19]*INFN - Gran Sasso Science Institute, L'Aquila I-67100, Italy*
[20]*Dipartimento di Scienze Fisiche e Chimiche, Università dell'Aquila, L'Aquila I-67100, Italy*
[21]*Centre de Spectrométrie Nucléaire et de Spectrométrie de Masse, 91405 Orsay Campus, France*
[22]*Massachusetts Institute of Technology, Cambridge, Massachusetts 02139, USA*
[23]*Physics Department, California Polytechnic State University, San Luis Obispo, California 93407, USA*
[24]*Department of Materials Science and Engineering, University of California, Berkeley, California 94720, USA*
[25]*Physics Division, Lawrence Berkeley National Laboratory, Berkeley, California 94720, USA*
[26]*Laboratorio de Fisica Nuclear y Astroparticulas, Universidad de Zaragoza, Zaragoza 50009, Spain*
[27]*Dipartimento di Scienze per la Qualità della Vita, Alma Mater Studiorum - Università di Bologna, Bologna I-47921, Italy*
[28]*Service de Physique des Particules, CEA/Saclay, 91191 Gif-sur-Yvette, France*
[29]*Lawrence Livermore National Laboratory, Livermore, California 94550, USA*
[30]*Department of Nuclear Engineering, University of California, Berkeley, California 94720, USA*
[31]*INFN - Sezione di Padova, Padova I-35131, Italy*
[32]*Dipartimento di Fisica, Università di Firenze, Firenze I-50125, Italy*
[33]*INFN - Sezione di Firenze, Firenze I-50125, Italy*
[34]*SUPA, Institute for Astronomy, University of Edinburgh, Blackford Hill, Edinburgh EH9 3HJ, United Kingdom*
[35]*Engineering Division, Lawrence Berkeley National Laboratory, Berkeley, California 94720, USA*
[36]*Dipartimento di Fisica e Astronomia, Alma Mater Studiorum - Università di Bologna, Bologna I-40127, Italy*

(Received 8 January 2016; published 25 April 2016)

We describe in detail the methods used to obtain the lower bound on the lifetime of neutrinoless double-beta ($0\nu\beta\beta$) decay in ^{130}Te and the associated limit on the effective Majorana mass of the neutrino using the CUORE-0 detector. CUORE-0 is a bolometric detector array located at the Laboratori Nazionali del Gran Sasso that was designed to validate the background reduction techniques developed for CUORE, a next-generation experiment scheduled to come online in 2016. CUORE-0 is also a competitive $0\nu\beta\beta$ decay search in its own right and functions as a platform to further develop the analysis tools and procedures to be used in CUORE. These include data collection, event selection and processing, as well as an evaluation of signal efficiency. In particular, we describe the amplitude evaluation, thermal gain stabilization, energy calibration methods, and the analysis event selection used to create our final $0\nu\beta\beta$ search spectrum. We define our high level analysis procedures, with emphasis on the new insights gained and challenges encountered. We outline in detail our fitting methods near the hypothesized $0\nu\beta\beta$ decay peak and catalog the main sources of systematic uncertainty. Finally, we derive the $0\nu\beta\beta$ decay half-life limits previously reported for CUORE-0, $T^{0\nu}_{1/2} > 2.7 \times 10^{24}$ yr, and in combination with the Cuoricino limit, $T^{0\nu}_{1/2} > 4.0 \times 10^{24}$ yr.

DOI: 10.1103/PhysRevC.93.045503

I. INTRODUCTION

Neutrinoless double-beta ($0\nu\beta\beta$) decay [1] is a hypothesized second-order weak decay in which a nucleus simultaneously converts two neutrons into two protons and produces only two electrons in the process, $(Z,A) \rightarrow (Z+2,A) + 2\beta^-$. The discovery of this decay would conclusively indicate that lepton number is violated and that neutrinos are Majorana fermions. Further, it could help constrain the absolute scale of the neutrino masses and their hierarchy [2], and would lend support to the theory that neutrinos played a fundamental role in the creation of the matter asymmetry of the Universe [3,4]. For all these reasons, the search for $0\nu\beta\beta$ decay has recently become the center of intense experimental effort utilizing a broad range of technologies [5–7]. At present, $0\nu\beta\beta$ decay has never been decisively observed, but several recent experiments have placed upper limits on its decay rate in ^{76}Ge [8], ^{136}Xe [9,10], and ^{130}Te [11].

The Cryogenic Underground Observatory for Rare Events (CUORE) [12,13] is a next-generation tonne-scale bolometric detector, currently in the advanced stages of construction at the Laboratori Nazionali del Gran Sasso (LNGS) of INFN and expected to begin operation in 2016. CUORE will search for the $0\nu\beta\beta$ decay of ^{130}Te using a segmented array of 988 TeO_2 bolometric detectors operated at extremely low temperatures. The detectors will be arranged into an array of 19 towers with 52 bolometers each for a total detector mass of 741 kg, or 206 kg of ^{130}Te.

CUORE builds on the experience of Cuoricino [14–16], which was a single tower of 62 bolometers with a total mass of ∼40 kg. Cuoricino ran from 2003–2008 and until recently held the best limits on the $0\nu\beta\beta$ decay half-life of ^{130}Te at $T^{0\nu}_{1/2} > 2.8 \times 10^{24}$ yr (90% C.L.) [16]. Moving from Cuoricino to CUORE, we seek to increase the active mass and improve sensitivity to $0\nu\beta\beta$ decay by reducing backgrounds through better material cleaning and handling [17–19]. The CUORE-0 detector is a single CUORE-style tower, with comparable active mass to Cuoricino, that was operated in the Cuoricino cryostat from 2013 to 2015. CUORE-0 serves as a technical prototype and validation of the background reduction techniques developed for CUORE, as well as a sensitive $0\nu\beta\beta$ decay search on its own.

This paper begins by briefly describing the design and operation of the CUORE-0 detector in Sec. II; a more detailed and technical description of the detector design and performance can be found in [20], and a report on the initial performance can be found in [21]. In Sec. III, we describe the production of the CUORE-0 energy spectrum; this process closely follows the one used for Cuoricino found in [16] (hereafter referred to as CINO2011), so here we focus on the parts of the analysis that have been further developed for CUORE-0, including the new data blinding procedure. In Sec. IV, we outline the data selection criteria and the signal efficiency evaluation. Section V summarizes our unblinding procedure. In Sec. VI, we present our technique for searching for a $0\nu\beta\beta$ decay signal and derive the limit on the half-life of $0\nu\beta\beta$ decay of ^{130}Te previously presented in [11]. In Sec. VII, we detail the performance of the CUORE-0 detector, particularly in comparison to the Cuoricino detector. In Sec. VIII we present the technique for combining the results of CUORE-0 and Cuoricino to obtain the limit on the $0\nu\beta\beta$ decay half-life of ^{130}Te presented in [11].

II. DETECTOR DESIGN AND DATA COLLECTION

The CUORE-0 experiment is a segmented array of 52 bolometric detectors arranged into a tower of 13 floors with four bolometers per floor [see Fig. 1(a)]. Each bolometer has three primary components: an energy absorber, a temperature sensor, and a weak thermal link to the copper frame that acts both as the structural tower support and the thermal bath [see Fig. 1(b)]. When energy is deposited in the absorber, its temperature increases suddenly by

$$\delta T = E/C(T), \quad (1)$$

*Present address: Physics Department, Princeton University, Princeton, NJ 08544, USA.
†cuore-spokesperson@lngs.infn.it
‡Deceased.

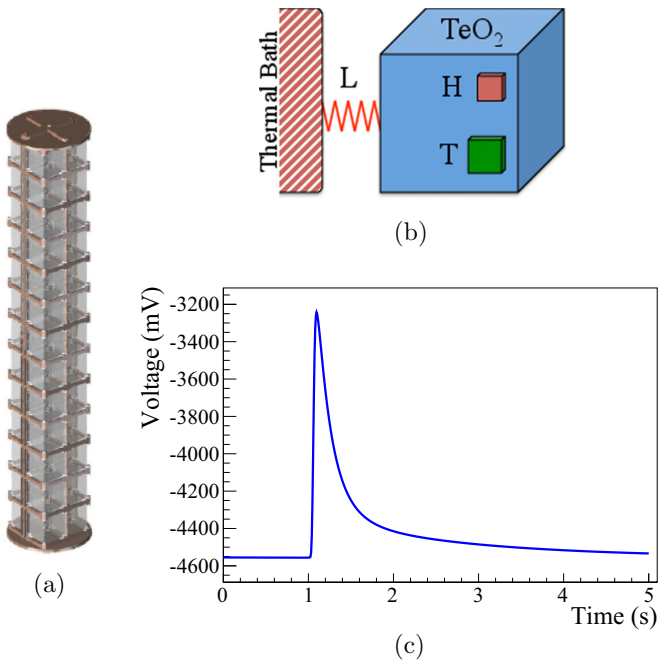

FIG. 1. (a) CUORE-0 tower array rendering. The tower consists of 13 floors of four bolometers, mounted in a copper frame. (b) Schematic of a single CUORE-0 bolometer showing the thermistor (T), the heater (H), and the weak thermal link (L) between TeO_2 crystal and copper thermal bath (not to scale). (c) An example of a bolometer signal with an energy of approximately 2615 keV. The rise and fall times of this signal are 0.05 s and 0.2 s, respectively. Figure from [21].

where $C(T)$ is the (temperature-dependent) heat capacity and E is the amount of energy deposited. As the energy slowly leaks out into the thermal bath, the bolometer gradually returns to its initial temperature. This temperature pulse is converted to a voltage pulse by the thermometer [see Fig. 1(c)] and by measuring its amplitude we can determine the amount of energy deposited in the bolometer.

In CUORE-0, the energy absorber is a 750 g $5 \times 5 \times 5\,\mathrm{cm}^3$ $^{\mathrm{nat}}TeO_2$ crystal which we cool to an operating temperature of $T_0 \approx 12$ mK. The typical heat capacity at this temperature corresponds to $\Delta T/\Delta E \sim 10$–$20\,\mu\mathrm{K/MeV}$. The natural isotopic abundance of ^{130}Te is $a_I = 34.167\%$ [22], thus the crystal acts as both the source of the decays of interest and detector of their energy. In this "source = detector" configuration, Monte Carlo simulations show that $\approx$88% of $0\nu\beta\beta$ decay events deposit all of their energy in the crystal in which the decay occurred. Thus the signal we are searching for is a monoenergetic peak at the Q value of the ^{130}Te decay, $Q_{\beta\beta} = 2527.518 \pm 0.013$ keV [23]. This energy is above that of the majority of the naturally occurring environmental γ radiation, but between the prominent 2615 keV line from the decay of ^{208}Tl and its Compton edge. In this region, the primary backgrounds are due to multiscattered γ events and degraded α decays which reach our detectors from the surfaces of materials near the crystals. A detailed description of the relevant backgrounds can be found in [24].

The CUORE-0 tower has a total active mass of 39.1 kg for a total ^{130}Te mass of 10.9 kg. The tower is cooled in the cryostat that housed the Cuoricino experiment. The cryogenic installation, shielding, and antiradon system are identical to Cuoricino (see [20] for details) and the backgrounds associated with this infrastructure is similarly unchanged (see Sec. VII).

We monitor the temperature of each bolometer by measuring the resistance of a neutron transmutation doped (NTD) Ge thermistor glued to each crystal. The NTD has a resistivity that is exponentially dependent on its temperature, making it a very sensitive thermometer [25–27]. We further instrument each crystal with a silicon resistor, which we use as a Joule heater to produce fixed-energy reference pulses for stabilizing the gain of the bolometers against temperature variations. Each bolometer is held in the copper frame with a set of polytetrafluoroethylene (PTFE) supports. These, as well as the 25 μm gold wires that instrument the NTD and Joule heater, form the weak thermal link to the thermal bath.

We bias each NTD through two low-noise load resistors and measure the output voltage signal using a specially designed low-noise room temperature preamplifier, a programmable gain amplifier, and a six-pole Thomson-Bessel low-pass filter with a programmable cutoff frequency set to 12 Hz. The data-acquisition system (DAQ) continuously samples each waveform at 125 S/s with $\pm$10.5 V dynamic range and 18 bit resolution. We trigger each data stream in software and store events in 5 s windows: the one second of data preceding the trigger and the four seconds after. Particle pulses—pulses coming from energy deposits in the crystals—have typical rise times of $\sim$0.05 s and two decay time components, a fast decay time of $\sim$0.2 s and a slower decay time of $\sim$1.5 s. The former decay time is determined by the heat capacity of the crystal and the thermal conductivity to the thermal bath, and the latter decay time by the heat capacity of the of the auxiliary components (i.e., the PTFE spacers and nearby copper frame). The rise time is determined primarily by the roll-off of the Bessel filter. Typical trigger thresholds range from 30 keV to 120 keV. Every 200 s, we collect 5 s waveforms simultaneously on all channels with no signal trigger and use these to study the noise behavior of the detector.

We collect data in 1-d-long runs, which are interrupted for 2–3 h every 48 h to refill the liquid He bath and perform other maintenance on the cryogenic system. Roughly once per month, we calibrate the energy response of the detector by inserting thoriated tungsten wires inside the external lead shielding and using the characteristic γ lines from the ^{232}Th decay chain. These calibration runs typically last for three days. The data are combined into datasets that contain roughly three weeks of $0\nu\beta\beta$ decay physics runs flanked at the beginning and the end by a set of calibration runs. Each crystal has a typical event rate of $\sim$1 mHz in the physics runs and $\sim$60 mHz in the calibration.

During the tower assembly, one NTD and one heater could not be bonded, and another heater was lost during the first cool down. Thus of the 52 bolometers, 49 are fully instrumented (working heater and thermistor), two are functional but without heater (thermistor only), and one cannot be read (no thermistor).

The detector was assembled in March 2012 and first cooled down in August 2012, with data collection starting in March 2013. The first data-taking campaign (Campaign I) lasted until September 2013 (8.5 kg yr of TeO_2, corresponding to 2.0 kg yr of ^{130}Te). We then paused data collection for about two months to perform maintenance on the cryostat. Data collection resumed in November 2013 and Campaign II lasted until March 2015. Combining both campaigns, the total exposure is 35.2 kg yr of TeO_2, corresponding to 9.8 kg yr of ^{130}Te.

III. FIRST-LEVEL DATA PROCESSING

The low-level data processing takes the CUORE-0 data from a series of triggered waveforms to a calibrated energy spectrum that will be the input into the higher-level analysis. The data processing procedure for CUORE-0 closely follows that of Cuoricino, outlined in CINO2011, but with several additions newly developed for CUORE-0.

In order to estimate the energy of each event, we model the time-waveform $v_i(t)$ of each bolometer, i, as the sum of a known detector response function $s_i(t)$ and an unknown additive noise term $n_i(t)$

$$v_i(t) = B_i\, s_i(t) + n_i(t), \tag{2}$$

where B_i is the amplitude of the signal response. To a very good approximation, this amplitude can be decomposed as

$$B_i = G_i(T) \cdot A_i(E), \tag{3}$$

where $A_i(E)$ depends only on the energy deposited into the bolometer E, and $G_i(T)$ is a bolometric gain which depends on the operating temperature of the bolometer T. The low-level data processing performs the following steps on each triggered waveform in order to extract the deposited energy:

(1) measure the amplitude of the signal B_i while minimizing the effect of the noise term in order to maximize the energy resolution of our detector (pulse amplitude evaluation);
(2) stabilize the temperature-dependent gain term $G_i(T)$ against temperature drifts of the detector (thermal gain stabilization);
(3) determine an energy calibration that models the form of $A_i(E)$, allowing us to extract the energy for each event (energy calibration);
(4) blind the region of interest (ROI) in order to prevent any bias in the later stages of our analysis (data blinding).

A. Amplitude evaluation

To evaluate the amplitude of the pulse B_i, we employ two parallel approaches. We apply the same optimum filtering (OF) technique described in [CINO2011, 28], as well as a new decorrelating optimum filter (DOF). Both filters are frequency-based and designed to maximize the signal-to-noise ratio (SNR), assuming a predetermined detector response function $s_i(t)$ and noise spectrum (see Fig. 2). These filters leverage the entire waveform to create an amplitude estimate rather than just a few points around the peak of the pulse.

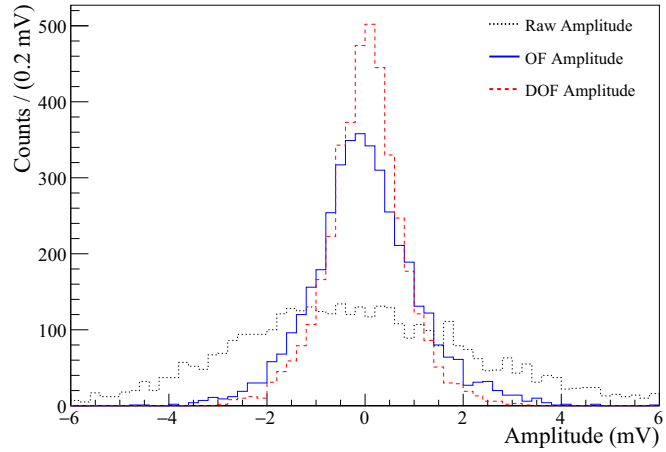

FIG. 2. The distribution of amplitudes of the noise pulses collected from a single channel during the physics data of a dataset from Campaign I. The widths of the above distributions are indicative of the amount of noise remaining after filtering. The channel presented is one where the DOF performed well. The raw unfiltered rms is 2.7 mV (black dotted histogram); the rms after OF is 1.1 mV (blue solid histogram); the rms after DOF is 0.8 mV (red dashed histogram).

Up to a multiplicative gain, an OF pulse can be written in frequency space as

$$V_i^{\mathrm{OF}}(\omega) \propto e^{i\omega t_{\max}} \frac{S_i^*(\omega)}{N_i(\omega)} V_i(\omega), \tag{4}$$

where $V_i(\omega)$ and $S_i(\omega)$ is the Fourier transform of the signal $v_i(t)$ and temporal detector response function $s_i(t)$, respectively, for bolometer i; $N_i(\omega)$ is the noise power spectral density of the underlying noise sources; ω is the angular frequency and $t_{\max}$ is the time at which the pulse reaches its maximum. The expected detector response $s_i(t)$ is computed for each bolometer over each dataset by averaging many events in the 2615 keV calibration line. The exact number of events depends on the counting rate and the amount of calibration data in a given dataset, but is typically several hundred events. The noise power spectral density $N_i(\omega)$ is similarly estimated for each bolometer on each dataset by averaging the noise power spectral densities of noise samples collected throughout each run.

The DOF generalizes Eq. (4) by accounting for noise correlations between neighboring bolometers [29,30]. The DOF pulse for an event on bolometer i is given by

$$V_i^{\mathrm{DOF}}(\omega) \propto e^{i\omega t_{\max}} \sum_j S_i^*(\omega) C_{ij}^{-1}(\omega) V_j(\omega), \tag{5}$$

where $C_{ij}^{-1}(\omega)$ is the i,j component of the inverted noise covariance matrix at frequency ω and the sum runs over a list of correlated bolometers. In CUORE-0, we limit this list to the 11 nearest geometric neighbors for bolometers in the middle floors of the tower (i.e., the four bolometers from the floor above, the four from the floor below, and the three on the same floor as the triggered bolometer) or the seven nearest neighbors for bolometers on the top and bottom floors. This filter can be thought of as working in two stages: it first subtracts the noise common to all bolometers and then

performs a regular OF on the bolometer of interest with the expected noise spectrum after removing common-mode noise. The key is that the neighboring bolometers provide an estimate of the common-mode noise. Note that if the covariance matrix is calculated with only the bolometer of interest and no neighboring bolometers [i.e., if $C_{ij}(\omega)$ is diagonal], then Eq. (5) reduces to Eq. (4).

The DOF typically outperforms the OF in reducing the rms of the noise in the physics runs but performs worse in the calibration runs. The higher event rate of the calibration runs leads to a higher probability of an event occurring on a neighboring bolometer within the 5 s triggered window which yields an incorrect estimate of the common-mode noise. This results in two scenarios: either the energy deposited is small (i.e., not much above the noise), the pulse goes untriggered, and is inadvertently included in the sum in Eq. (5); or the event is triggered and the waveform is excluded from the sum and the filter is no longer "optimal" (i.e., the terms in the sum are not optimized for the smaller set of bolometers). Both scenarios degrade the performance of the DOF.

This effect is only prominent in the calibration runs where the event rate is about 60 times higher than in the physics runs and thus, in theory, does not worsen the DOF performance on the physics data and in our $0\nu\beta\beta$ analysis. However, as we show in Sec. VI, the calibration runs are essential to determining the energy resolution input to our $0\nu\beta\beta$ decay analysis, so this makes the DOF problematic. Despite this, for some bolometers, the benefit of the decorrelation outweighs the degradation due to the higher event rate in the calibration data. Thus the final CUORE-0 dataset utilizes both the OF and the DOF, depending on which performed better on the 2615 keV ^{208}Tl line in the calibration data. In order to use the DOF over the OF the improvement in energy resolution at 2615 keV must be statistically significant at the $\gtrsim$90% level. With this requirement, 20% of the final CUORE-0 data production utilizes the DOF.

Once filtered, the amplitude of each pulse is determined by interpolating the three data points around the peak of the filtered pulse and evaluating the maximum of that parabola.

B. Thermal gain stabilization

The thermal gain stabilization (TGS) compensates slow variation in the gain of the bolometers $G_i(T)$ due to drifts of the operating temperature of the detector. As with the amplitude evaluation, we use two techniques in parallel: a heater-based TGS and a calibration-based TGS.

The heater-TGS is identical to the technique described in CINO2011 and described further in [31]. This approach uses the heater attached to each bolometer to inject fixed-energy reference pulses every 300 s during each run. Since the energy of the reference pulse is constant, any variation in its measured amplitude B_i^{ref} is due to a change in the bolometric gain $G_i(T)$. We use the average value of the baseline, measured in the one second of data preceding the trigger, as a proxy for the bolometer temperature at the time of the event. By regressing the reference amplitude B_i^{ref} as a function of the baseline value, we can determine $G_i(T)$—up to a multiplicative constant that can be folded into $A_i(E)$. We then factor $G_i(T)$ out of the measured amplitude B_i to stabilize our bolometric response against thermal drifts.

For the two bolometers without functioning pulser heaters the heater-TGS cannot be applied. These two bolometers amount to about 4% of our total exposure. Moreover, for some bolometers the heater-TGS algorithm consistently failed to stabilize the gain over very large temperature drifts. This was due partly to deviations from linearity and partly to differences in the way energy is deposited by particle interactions versus heater pulses (i.e., differences in the pulse shapes resulting from particle interactions and heater pulses). A failure of the heater-TGS manifests as a shift in the location of the calibration peaks between the initial and final calibration runs, visible as two distinct peaks in the calibration spectrum. In this case, we consider the entire dataset invalid for that particular bolometer. These shifted calibration datasets correspond to about 7% of our total exposure.

In order to address these issues, we developed a TGS algorithm based on calibration data and independent from the heater. This approach uses the 2615 keV γ line in the calibration runs in lieu of the monoenergetic pulser to map the temperature-dependent gain $G_i(T)$. We regress the gain dependence measured in the calibration runs (see Fig. 3) and use this to correct the amplitudes of events in both the calibration and physics runs. Since calibration-TGS is interpolated across an entire dataset, it requires carefully measuring and accounting for the applied and stray voltage offsets. This calibration-TGS allowed us to recover about 80% of the lost exposure on the two bolometers with broken heaters. Additionally, in cases of large temperature drifts, the calibration-TGS routinely outperformed the heater-TGS and resulted in little or no shift between the peak positions in the

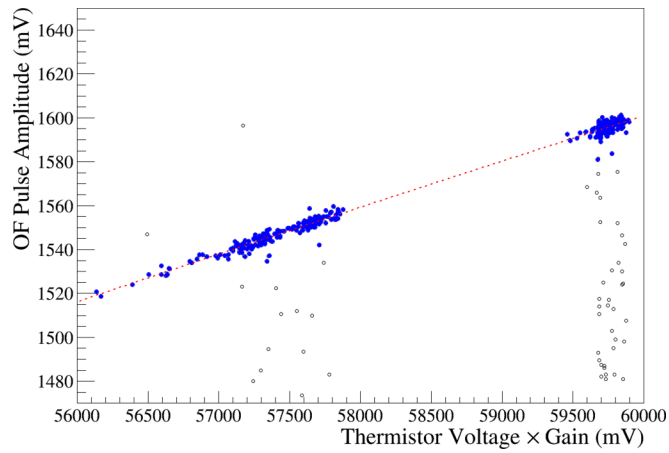

FIG. 3. Example of the calibration-TGS. The points are taken during the calibration runs for one of the CUORE-0 datasets. The cluster of points on the right are from the calibration runs which opened the dataset, while the cluster on the left are from the closing calibration runs. The solid blue points have energies around the 2615 keV ^{208}Tl peak and are used for calibration-TGS. By regressing the measured amplitudes of these points against the NTD voltage we can determine a stabilization curve (*red dashed line*) which is then applied to the physics runs taken between calibrations.

initial and final calibration runs, as measured on the 2615 keV line. This allowed us to recover much of the 7% of exposure that would have been rejected with the heater-TGS; and further it improved the resolution of other bolometers that showed a marginal peak shift between initial and final calibration runs, but one not large enough to be considered invalid. All told, we used the calibration-TGS on 12% of the total CUORE-0 exposure.

For the majority of the CUORE-0 data, applying the TGS caused temperature-dependent gain drifts to become a subleading cause of degradation in the energy resolution of our detector. However, in 2.7% of the final exposure both TGS algorithms failed significantly, usually due to an abnormally large or sudden drift in temperature or a change in electronic operating conditions. These data were discarded for the rest of the analysis.

C. Energy calibration

For each dataset, we calibrate the energy response of each bolometer $A_i(E)$ using the reconstructed positions of at least four of the seven strongest γ peaks from the ^{232}Th decay chain. This consists of fitting each peak position using a Gaussian lineshape plus a first degree polynomial background and performing a linear regression on the expected energies of the calibration peaks against their reconstructed positions using a second-order polynomial with zero intercept.

In Sec. VI, we show that a Gaussian line shape does not provide a good fit to the reconstructed peak shapes. This discrepancy leads to a small bias in the reconstructed event energies, but rather than correcting for this bias at the calibration stage, we adjust the position at which we search for a $0\nu\beta\beta$ decay signal (this is detailed in Sec. VI). For CUORE, we plan to improve our energy reconstruction by accounting for these non-Gaussian peak shapes during the data processing.

D. Data blinding

The final step of the first level data processing is the blinding of the ROI. Our blinding procedure is designed to mask any possible signal or statistical fluctuation at $Q_{\beta\beta}$, while maintaining the spectral integrity so that we can use the blinded energy spectrum for testing our later analyses. We use a form of data salting that randomly shifts the reconstructed energy of a fraction of events from within 10 keV of the ^{208}Tl 2615 keV peak by -87 keV to around $Q_{\beta\beta}$ and the same fraction of events from within 10 keV of $Q_{\beta\beta}$ by $+87$ keV to around the ^{208}Tl peak. Because there are significantly more events around the ^{208}Tl peak, this creates an artificial peak at $Q_{\beta\beta}$ with the shape of a true signal peak. The fraction of events is blinded and random but chosen from a range such that the artificial peak is unrealistically large [see Fig. 7(b)]. Each event's true energy is encrypted and stored, to be decrypted later during unblinding. This procedure is pseudorandom and repeatable. The calibration runs are not blinded. The steps for unblinding are detailed in Sec. V.

IV. DATA SELECTION AND SIGNAL EFFICIENCY

A. Data selection

Once the first level data processing is complete, we select the events of interest with a set of event cuts. These cuts fall into three types:

(1) Time-based cuts that remove periods of time where the data quality were poor or the data processing failed.
(2) Event-based cuts that remove poorly reconstructed and non-signal-like events to maximize sensitivity to $0\nu\beta\beta$ decay.
(3) Anticoincidence cuts that remove events that occur in multiple bolometers and are thus less likely to come from a $0\nu\beta\beta$ decay.

1. Time-based selection

The first set of cuts removes intervals of time where the data collection was poor. This typically removes periods of excessive noise from an individual bolometer (e.g., a malfunctioning electronic channel), or periods of time when the entire detector temperature was fluctuating quickly (e.g., during an earthquake). This cut introduces a dead time that reduces our total exposure by 3.5%. We further remove intervals of time when the data processing failed. The most significant component of this was a failure of the TGS algorithms to stabilize gain variations over too large a temperature drift. These excluded periods lead to the reduction in our total exposure of 2.7% mentioned in the previous section.

2. Event-based selection

We implement a set of event based cuts that remove events that are either non-signal-like or are in some way not handled well by the data processing software. This includes a set of basic quality cuts that removes events that are clearly problematic, such as events that exceed the dynamic range of the electronics or events that overlap with one of the injected heater pulses. We further implement a pile-up cut that rejects an event if more than one trigger occurs in the same bolometer within 3.1 s before or 4 s after the event trigger. This 7.1 s window allows any previous event enough time to return to baseline and ensures that any following event does not occur within the event window.

In addition to these basic quality checks, we have developed a set of pulse shape cuts, which remove events on the basis of six pulse shape parameters. These include the slope of the baseline as well as the time in the event window that the signal reaches its maximum. Cutting on these two parameters is useful for removing events whose amplitudes are poorly reconstructed by the processing software. The pulse shape cuts also cut on the pulse rise and decay times, which are useful for identifying pile-up events that failed to cause a second trigger and events that have very fast time constants and are believed to be due to energy depositions in the thermistor itself, fast temperature variations due to vibrations, or electronic noise. The last pulse shape cut selects on two parameters referred to as "Test Value Left" (TVL) and "Test Value Right" (TVR). These are effectively χ^2 values between the normalized OF filtered pulse shape and the expected filtered detector response

TABLE I. CUORE-0 signal detection efficiency. See the text for how these are calculated.

Source	Signal efficiency (%)
$0\nu\beta\beta$ energy confinement	$88.345 \pm 0.040(\text{stat}) \pm 0.075(\text{syst})$
Trigger & reconstruction	98.529 ± 0.004
Pile-up & pulse shape cuts	93.7 ± 0.7
Anticoincidence cut	99.6 ± 0.1
Total	81.3 ± 0.6

shape on either the left or right side of the signal peak. These last two parameters are useful for identifying events whose shape deviates significantly from the expected detector response shape.

All pulse shape parameters have an energy dependence, which we normalize by interpolating across events that lie within peaks in the calibration spectrum over the range 146 keV to 2615 keV. As a result, the efficiency of the cuts on these variables is independent of energy to within statistical uncertainty over this range. We tune these pulse shape cuts by maximizing the signal efficiency over the square root of the background in the physics spectrum, where the signal efficiency is measured as the fraction of selected events in the γ peaks over the range 146–2615 keV, and the background is measured in the energy regions around the peaks. To avoid biasing our selection, we use a randomly selected half of the data for tuning the selection and the remaining events for determining the selection efficiency (reported in Table I). We exclude the $0\nu\beta\beta$ decay ROI from both calculations.

3. *Anticoincidence selection*

Since the desired $0\nu\beta\beta$ decay events have their full energy absorbed in a single bolometer, we use an anticoincidence cut to reject any event that occurs within ± 5 ms of another event in any other bolometer in the tower. This cut primarily rejects α decays that occur on the surfaces of our bolometers, γ rays that scatter in one bolometer before being absorbed in another, cascade γ rays from radioactive decays, and muons passing through the tower and their secondary neutrons. A plot of the energies of double-crystal coincidence events—events where two bolometers are triggered—is shown in Fig. 4. In CINO2011, the anticoincidence window was ± 50 ms, and in [21] we used a window of ± 100 ms. Here we have significantly narrowed this window by accounting for the constant differences in detector rise times between different bolometers when measuring the time between two events on different bolometers (see Fig. 5). This correction improves the timing resolution by a factor of ≈ 50.

After implementing all cuts, 233 out of 411 triggered events remain in the ROI for the $0\nu\beta\beta$ analysis described in Sec. VI.

B. Signal detection efficiency

The signal detection efficiency for a $0\nu\beta\beta$ decay is a product of conditional probabilities: the probability that the full energy of the decay is contained in a single crystal, the probability that the event is then triggered and properly reconstructed,

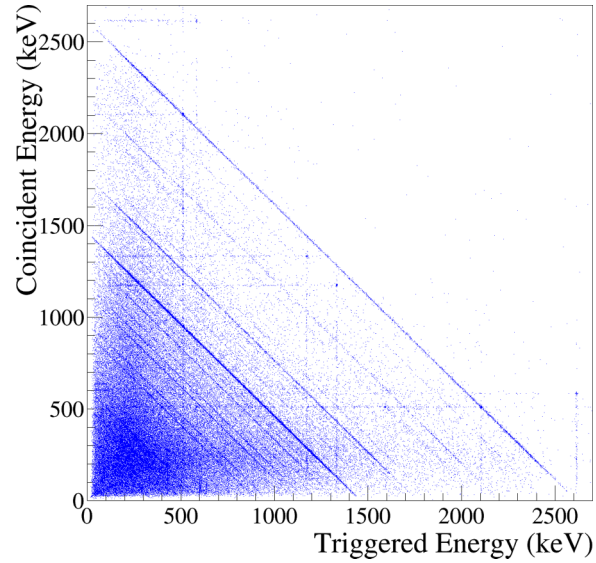

FIG. 4. Plot of the two absorbed energies in double-crystal coincidences during physics data collection. The diagonal lines correspond to events where a γ scatters in one crystal and is then fully absorbed in another. The vertical and horizontal lines are cascade events where one γ is fully absorbed and the other is scattered. This can be seen for the two ^{60}Co γ rays, ^{208}Tl 2615 keV +583 keV γ rays, and ^{208}Tl pair production events where one annihilation photon escapes and is absorbed in another bolometer.

the probability that the event then passes the signal cuts, and the probability that the event is not then accidentally in coincidence with an unrelated event in a different bolometer. These efficiencies are summarized in Table I.

We use a GEANT4-based [32] Monte Carlo simulation to estimate the fraction of events that deposit their full energy in a single crystal. This simulation models the most significant energy loss mechanisms: electron escape, x-ray escape, and the escape of Bremsstrahlung photons. The simulation also

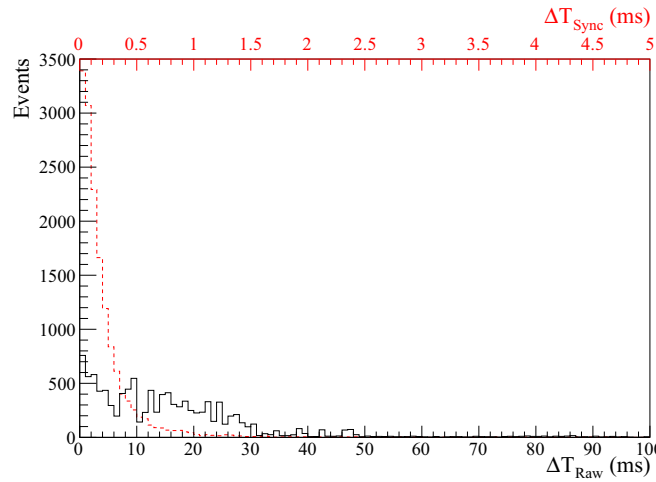

FIG. 5. Distribution of measured time between coincident events before correcting for different detectors' rise time (black solid, ΔT_{Raw}) and after (red dashed, ΔT_{Sync}).

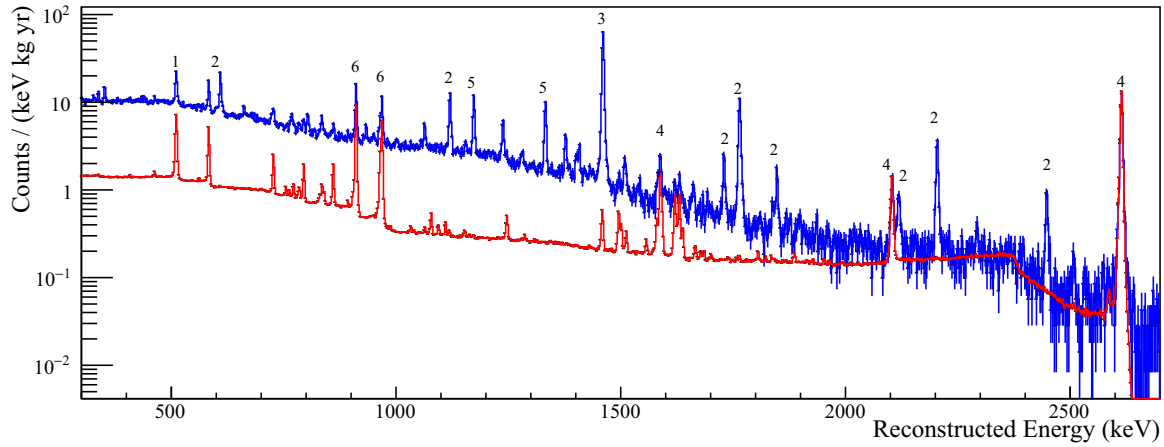

FIG. 6. The final CUORE-0 physics spectrum (blue) and calibration spectrum (red). The calibration spectrum has been normalized to match the rate of the physics spectrum around the 2615 keV ^{208}Tl peak. The most prominent peaks in the physics spectrum are from the decay of known radioactive backgrounds: (1) e^+e^- annihilation, (2) ^{214}Bi, (3) ^{40}K, (4) ^{208}Tl, (5) ^{60}Co, and (6) ^{228}Ac. Figure adapted from [11].

mimics the detector response by convolving the spectrum with a Gaussian to reproduce the expected shape near $Q_{\beta\beta}$. We calculate the efficiency by fitting the resulting $0\nu\beta\beta$ decay peak and dividing the fitted area by the number of simulated decays. The efficiency evaluates to $88.345 \pm 0.040(\text{stat}) \pm 0.075(\text{syst})\%$. The systematic uncertainty is from the variation in the crystal dimensions, the uncertainty in decay energy, and the step choice for secondary propagation in the GEANT4 simulation.

We evaluate the trigger and energy reconstruction efficiencies using the pulser heater events. The DAQ automatically flags each heater event in the data, and then passes the event through the standard signal trigger algorithm. The fraction of heater events that also generate a signal trigger provides an estimate of our signal trigger efficiency. The heater events typically reconstruct as a Gaussian peak around 3–3.5 MeV. We determine our energy reconstruction efficiency by fitting this heater peak with a Gaussian line shape and counting the fraction of events that reconstruct within 3σ. This calculation is done for each bolometer for each physics run and averaged, weighted by exposure, to determine a single efficiency for the entire detector. The bolometers without working heaters are excluded from this calculation and are assigned the same efficiency as the other bolometers—thus they are assumed to have the average efficiency of the other bolometers.

We estimate the efficiency of the signal cuts (i.e., pile-up and pulse shape) using the ^{208}Tl 2615 keV peak in the physics data. The vast majority of events that reconstruct in the peak are properly reconstructed; pile-up events and events with nonstandard pulse shapes reconstruct somewhat randomly with a much wider distribution. We estimate our cut efficiency by measuring the rate within 5σ of the 2615 keV peak and subtracting the background rate measured in bands around the peak. We compare this signal rate before and after applying the cuts to determine the fraction of signal events that are accidentally removed by the signal cuts.

The anticoincidence efficiency accounts for the rejection of valid events due to an event being close enough in time to an unrelated event on another bolometer so as to accidentally be considered a coincidence. This efficiency is estimated in a similar fashion to the signal cut efficiencies—comparing the signal rate before and after the cut—except that it is calculated around the 1460 keV line from electron capture in ^{40}K. While the ^{208}Tl 2615 keV γ ray can be part of cascade and is expected to occasionally occur in coincidence with other γ rays, the ^{40}K 1460 keV only occurs in coincidence with a 3 keV x ray which is well below the trigger threshold of our bolometers. Thus any event in coincidence with a fully absorbed 1460 keV γ ray constitutes an accidental coincidence.

Combining these, we determine the total signal efficiency of the CUORE-0 detector to be $81.3 \pm 0.6\%$.

V. DATA UNBLINDING

The unblinding procedure was decided upon before any data were unblinded. After fixing the data selection cuts and the $0\nu\beta\beta$ decay analysis procedure (described in the next section), we unblinded the data in two stages: first we unblinded 17 of 20 datasets (or 8 kg yr of ^{130}Te exposure) and began the $0\nu\beta\beta$ decay analysis while we continued to collect the final three datasets (or 1.8 kg yr of ^{130}Te exposure). The last three datasets were blinded during collection, were subjected to the same production procedure and cuts as the rest of the data, and were to be included regardless of their effect on the final result. The unblinded spectrum is shown in Fig. 6, and the blinded and unblinded spectra in the ROI are shown in Fig. 7(b).

As a crosscheck, we also reproduced all of the CUORE-0 data without the blinding/unblinding steps and compared them to the data that had been blinded and unblinded to confirm it had no effect on the final spectrum. Indeed, the blinding/unblinding procedure had no effect on our final spectrum. This confirmation of our blinding/unblinding procedure validates this technique moving forward to CUORE.

VI. $0\nu\beta\beta$ ANALYSIS

The CUORE-0 physics spectrum over the range 300–2700 keV is shown in Fig. 6. The CUORE-0 data consists of 20 datasets collected on 51 active bolometers. After implementing

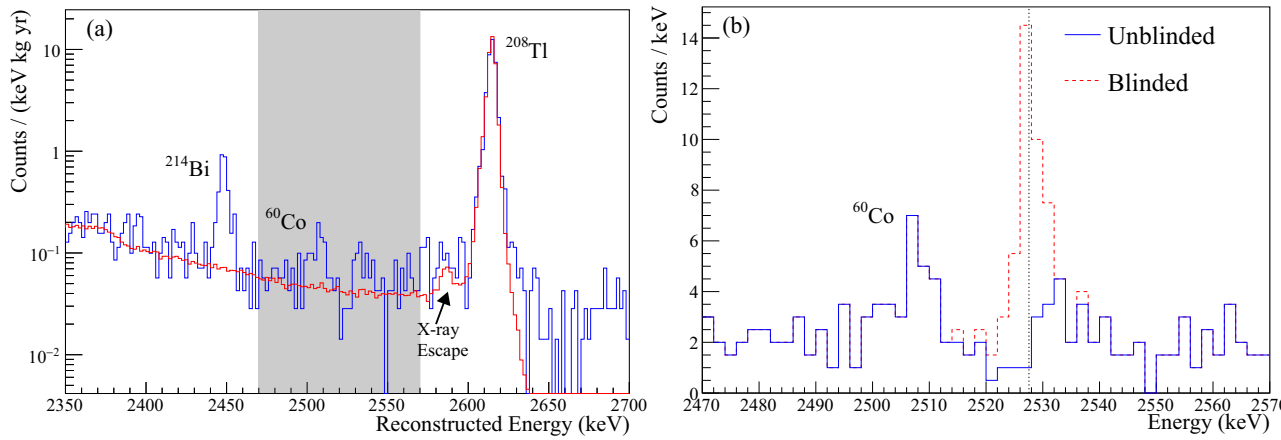

FIG. 7. (a) The CUORE-0 spectrum around the ROI. This is a zoomed view of Fig. 6. The shaded region corresponds to the energy range used in the ROI fit. The background in the ROI is now dominated by the scattered-γ background rather than the flat α background. (b) Comparison of the blinded (dashed lines) and unblinded (solid lines) spectra in the ROI. The peak in the dashed spectrum is the artificial peak created by the blinding procedure. $Q_{\beta\beta}$ is indicated by the dotted line.

all cuts, 1008 bolometer-dataset (BoDs) pairs remain for a total TeO_2 exposure of 35.2 kg yr, or 9.8 kg yr of ^{130}Te. Our $0\nu\beta\beta$ decay analysis treats each one of these as a semi-independent experiment with some parameters unique to each BoDs, some parameters shared across datasets (i.e., constant in time), and other parameters shared globally (i.e., constant in time and uniform across the detector).

We define the ROI for our $0\nu\beta\beta$ decay analysis as the range 2470–2570 keV; this region contains 233 events. This is the widest possible range that allows us to constrain the background rate without introducing unnecessary peaks into the analysis. The range is bounded by a ^{214}Bi line at 2448 keV and a small peak at 2585 keV from a 2615 keV ^{208}Tl γ ray minus a 30 keV Te x-ray escape [see Fig. 7(a)]. The ROI contains the potential $0\nu\beta\beta$ decay signal at 2527 keV as well as a peak from the single-crystal coincidence of the two γ rays from ^{60}Co decay which lies only 21 keV below. We attribute this ^{60}Co contamination to the activation of the copper frames and internal shielding [24]. We have measured the production rate of ^{60}Co inside the TeO_2 crystals to be small [33], so we expect a negligible background from the $\beta+\gamma+\gamma$ coincidence.

Our $0\nu\beta\beta$ decay analysis proceeds through three steps. We first construct a detector response function ρ_i for each BoDs, which characterizes the expected spectral shape of a particular bolometer's response to a monoenergetic energy deposition during a particular dataset. We then use this set of ρ_i to fit other prominent peaks in the physics spectrum. This allows us to understand how our detector response depends on energy. Finally, we fit the ROI by postulating a peak at the $0\nu\beta\beta$ decay energy and constraining its amplitude with a detector response function properly scaled in energy. The resulting best-fit amplitude provides insight into the $0\nu\beta\beta$ decay rate.

A. Detector energy response

We model the detector response to the monoenergetic $0\nu\beta\beta$ decay signal based on the measured response to the γ peaks. This is done for each BoDs, i, using the functional form

$$\rho_i(E;\mu_i,\sigma_i,\delta_i,\eta_i) \equiv (1-\eta_i)\text{Gauss}(E;\mu_i,\sigma_i) + \eta_i\text{Gauss}(E;\delta_i\mu_i,\sigma_i). \quad (6)$$

This function produces a primary Gaussian centered at μ_i and a secondary Gaussian at a slightly lower energy $\delta_i\mu_i$, with $\delta_i \sim 0.997$. This smaller secondary peak accounts for $\eta_i \sim 5\%$ of events and models an energy loss mechanism whose origin is presently under investigation. The presence of this substructure is unaffected by the choice of pulse filtering technique or TGS algorithm and is present on all channels. It is not clustered in time or a result of pile-up of events. It also does not appear to be correlated with any shape parameter used in the above cuts. A visual inspection of pulses selected from the primary and secondary peaks reveals no obvious difference in the pulse shape. The Cuoricino data show a hint of this asymmetric line shape; however, it is the improved resolution of the CUORE-0 detector that has made this effect clear. We tested multiple models to reproduce the line shape, including a Gaussian distribution with an asymmetric tail and a triple Gaussian lineshape which modeled escapes of 4 keV characteristic x rays from Te. Ultimately, we settled on the double-Gaussian shape which reproduced the data well across a broad range of energies.

Each BoDs has its own peak position, μ_i, and a single resolution parameter, σ_i, for both the primary and secondary Gaussian peaks. The data suggest that the position and amplitude of the secondary Gaussian peak may vary between bolometers and in time, thus indicating that this is possibly a detector related effect. Both δ_i and η_i are free to vary from bolometer to bolometer, but to limit the number of free parameters both are constant in time within each of the two data-taking campaigns.

We estimate the best-fit detector response for each BoDs by fitting the intense ^{208}Tl 2615 keV calibration peak. This fit is over the range 2560–2650 keV and includes three more elements to model the background under the detector response: (i) a smeared step function, modeled as an Erfc function, to

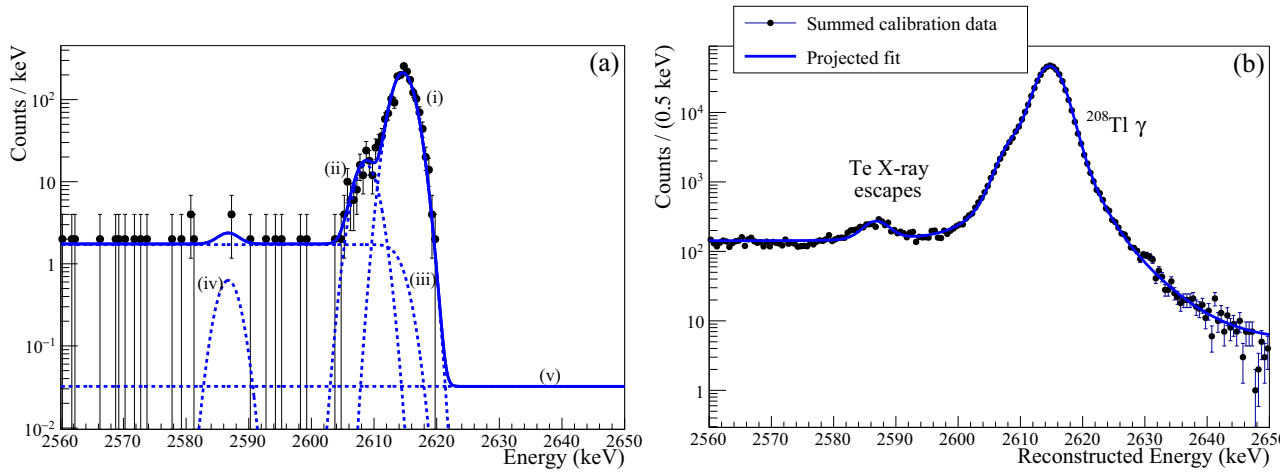

FIG. 8. (a) Best-fit model to the calibration 2615 keV peak for a single bolometer dataset. The solid line shows the full summed model, and the dashed lines show the individual components: (i) the primary peak of the detector response; (ii) the secondary peak of the detector response; (iii) the smeared step-function; (iv) the x-ray escape peak; (v) flat background. (b) The calibration spectrum summed over all BoDs pairs, with the summed best-fit model. Figure adapted from [11].

model γ rays that scatter in the shields before interacting with a bolometer or scatter multiple times in a single bolometer before exiting; (ii) a Gaussian peak roughly 30 keV below the primary peak to model an event in which a 2615 keV γ ray is absorbed and one of the characteristic Te K shell x rays, which have energies that range from 27–31 keV, is produced and escapes the crystal; (iii) a flat background. The best fit for a single BoDs is shown in Fig. 8(a).

The full calibration peak model is given by

$$f_i^{\mathrm{Tl}}(E) = R_i^{\mathrm{Tl}}\rho_i(E;\mu_i,\sigma_i,\delta_i,\eta_i) + r_{\mathrm{Scatter}}R_i^{\mathrm{Tl}}\mathrm{Erfc}\left(\frac{E-\mu_i}{\sqrt{2}\sigma_i}\right) + r_{\mathrm{Escape}}R_i^{\mathrm{Tl}}\mathrm{Gauss}(E;\delta_{\mathrm{Escape}}\mu_i,\sigma_i) + b^{\mathrm{Cal}}, \quad (7)$$

where R_i^{Tl} represents a BoDs dependent ^{208}Tl peak event rate in counts/(kg yr), which is a free parameter in the fit. The event rates of both the scattered γ rays and the x-ray escape peak are given as fractions of the peak event rate, r_{Scatter} and r_{Escape}, respectively. Both of these are global physical parameters that could be estimated using Monte Carlo, but since modeling them requires carefully accounting for detector thresholds (to accurately predict the fraction that are flagged as a coincidence) these parameters are instead left unconstrained in the fit. The position of the x-ray escape peak is described as a fraction of the primary peak energy, δ_{Escape}, and is also left unconstrained in the fit. The final parameter b^{Cal} is a global flat background rate in counts/(keV kg yr), also unconstrained.

We perform a simultaneous unbinned extended maximum likelihood (UEML) fit to all BoDs pairs using the ROOFIT fitting package [34]. For each BoDs, this yields a set of parameters which describe the detector response function, $(\hat{\mu}_i,\hat{\sigma}_i,\hat{\delta}_i,\hat{\eta}_i)$. We fix these parameters for use later in the ROI fit. Figure 8(b) shows the resulting best-fit model to the summed calibration data over all BoDs pairs.

B. Detector response as a function of energy

For each BoDs, we consider the parameters that characterize the detector response at 2615 keV, $(\hat{\mu}_i,\hat{\sigma}_i,\hat{\delta}_i,\hat{\eta}_i)$, as fixed. By fitting this detector response to other γ lines in the physics spectrum, we can derive the energy dependence of the detector response, in particular the predicted response at $Q_{\beta\beta}$. Specifically, we seek to account for

(i) any bias in the reconstructed energy of a $0\nu\beta\beta$ decay signal;
(ii) the dependence on energy of the detector energy resolution.

Since the 2615 keV peak lies only 87 keV above $Q_{\beta\beta}$, we use it as an anchor for our ROI fit. Most importantly, for each BoDs we use the reconstructed energy of the ^{208}Tl peak in the calibration data to dictate the energy at which we search for a $0\nu\beta\beta$ decay peak, i.e., rather than fixing our fit position to $Q_{\beta\beta}$, we search for a peak 87 keV below $\hat{\mu}_i$ in each BoDs; this allows us to decrease the impact of any residual miscalibration. For this, we analyze the prominent γ lines in the physics spectrum over the energy range 300–2500 keV.

Anticipating the approach to fitting the ROI described in the next section, we take an analogous approach to fitting the γ peaks in the physics spectrum. For each γ line, we perform an UEML fit with the position of the detector response shifted down from the ^{208}Tl peak position, $\hat{\mu}_i \to \hat{\mu}_i - \Delta$, and all of the energy resolutions scaled by a fixed amount, $\hat{\sigma}_i \to \alpha_\sigma\hat{\sigma}_i$. The shift in energy Δ parametrizes the difference in energy between the reconstructed peak in the physics spectrum and the reconstructed ^{208}Tl peak in the calibration spectrum. The scaling of the energy resolution α_σ parametrizes the resolution scaling both as a function of energy and between the calibration and physics data. In the fit, both parameters are unconstrained and the same for all BoDs pairs. The parameters of the secondary peak, δ_i and η_i, are held fixed. Each fit also includes a background model that is either a first or second-degree

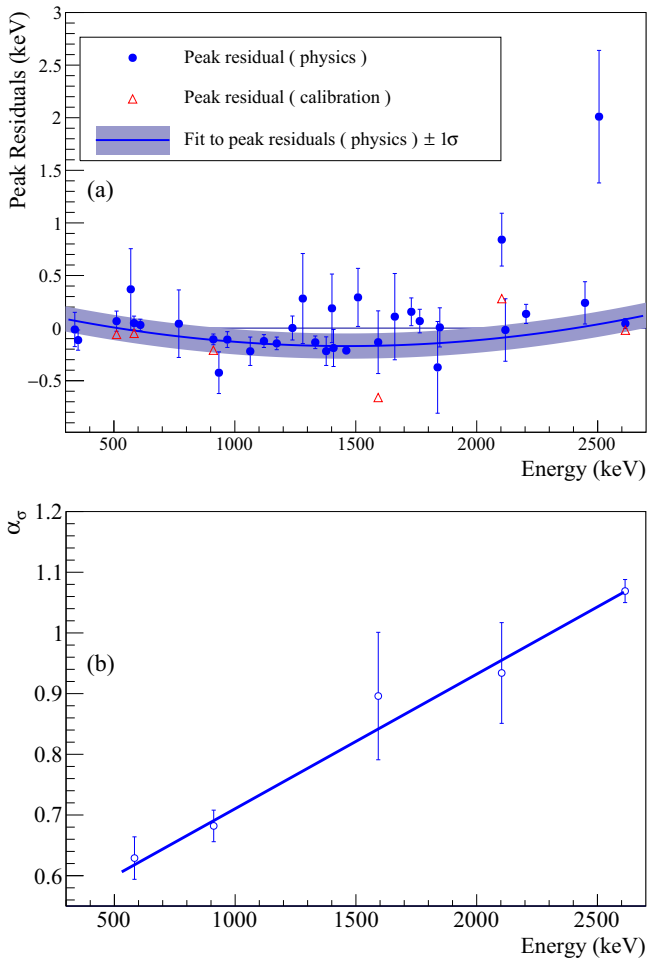

FIG. 9. (a) Residuals of the best-fit reconstructed peak energy and expected peak energy (fit–expected) for the physics data (blue circles) and calibration data (red triangles)—the statistical errors on the calibration points are negligible. The blue curve and shaded band are the fit to the physics peak residuals $\Delta\mu(E)$ and the 1σ uncertainty band. Figure adapted from [11]. (b) Best-fit resolution scaling parameter, α_σ, for a few of the peaks in the physics spectrum, as well as the best-fit interpolation.

polynomial. Including Δ and α_σ, each fit has four to five free parameters.

For each peak, we compare the best-fit shift from the ^{208}Tl calibration peak to the expected shift for that peak to determine its energy reconstruction residual $\Delta\mu$. The residuals for 33 prominent peaks in the physics spectrum and six peaks in the calibration spectrum are shown in Fig. 9(a). Note that these residuals are relative to the 2615 keV peak in the calibration data, thus include any residual miscalibration both as a function of energy and between the calibration and physics spectra. The residuals display a parabolic energy dependence, which we attribute to a systematic bias in the energy calibration step of the data processing.

We account for this systematic miscalibration by shifting the position at which we expect our $0\nu\beta\beta$ decay signal to occur. We fit a second-order polynomial to the peak residuals, $\Delta\mu(E)$, and evaluate the expected residual at the ^{130}Te Q value, and use the weighted rms of the residuals about $\Delta\mu(E)$ as the systematic uncertainty, $\Delta\mu(Q_{\beta\beta}) = 0.05 \pm 0.05\,(\text{stat}) \pm 0.09\,(\text{syst})$ keV. As is evident from Fig. 9(a) the ^{60}Co single-crystal coincidence peak shows a higher than expected residual and so this peak as well as the ^{208}Tl single-escape peak at 2103 keV are excluded from the evaluation of $\Delta\mu(E)$; we comment further on these peaks in Sec. VII.

We perform a similar interpolation to estimate the energy resolution scaling at $Q_{\beta\beta}$, which evaluates to $\alpha_\sigma(Q_{\beta\beta}) = 1.05 \pm 0.05$ [see Fig. 9(b)]. As above, this scaling includes both an energy dependent component as well as any bias between the calibration and physics data. The uncertainty on this scaling is purely systematic, and driven by the choice of γ lines to include in the fit. For the central value quoted here, we include only the γ peaks that are well defined in both the physics and calibration spectra.

C. Fitting the region of interest

The fit to the ROI follows an analogous process to the other peaks in the physics spectrum. We simultaneously fit both the hypothetical $0\nu\beta\beta$ decay signal and the peak from the single-crystal ^{60}Co coincidence. For each BoDs, we model the ROI as

$$f_i(E) = R^{0\nu}\rho_i\left(E; E_i^{0\nu}, \alpha_\sigma(Q_{\beta\beta})\hat{\sigma}_i, \hat{\delta}_i, \hat{\eta}_i\right) + R^{\text{Co}}(t)\rho_i\left(E; E_i^{\text{Co}}, \alpha_\sigma(Q_{\beta\beta})\hat{\sigma}_i, \hat{\delta}_i, \hat{\eta}_i\right) + b_{\text{ROI}}, \quad (8)$$

where $R^{\text{Co}}(t)$ and $R^{0\nu}$ are the event rates in counts/(kg yr) for ^{60}Co and $0\nu\beta\beta$ decay and are assumed to be uniform across the detector. We account for the 5.3 yr half-life of ^{60}Co by parametrizing $R^{\text{Co}}(t) = R^{\text{Co}}(0)e^{-t/\tau_{\text{Co}}}$, where $R^{\text{Co}}(0)$ (a free parameter in the fit) is the ^{60}Co decay rate at $t = 0$ which corresponds to the start of data-taking in March 2013 and τ_{Co} is the ^{60}Co lifetime. For each BoDs, we fix the location of the $0\nu\beta\beta$ decay signal at $E_i^{0\nu} \equiv \hat{\mu}_i - 87.00 + \Delta\mu(Q_{\beta\beta})$, which is the expected location of a potential $0\nu\beta\beta$ decay signal after correcting for the small residual calibration bias. The position of the ^{60}Co peak is handled identically to the other peaks in the physics spectrum: we parametrize $E_i^{\text{Co}} \equiv \hat{\mu}_i - \Delta$, with Δ left unconstrained in the fit. We model the background as constant in energy over this range, with b_{ROI} giving the rate in counts/(keV kg yr), common for all BoDs pairs and unconstrained in the fit. We test other possible background shapes (i.e., linear and parabolic) as part of our systematic study.

We can directly relate $R^{0\nu}$ to the physical ^{130}Te $0\nu\beta\beta$ decay rate $\Gamma_{0\nu}$ through

$$R^{0\nu} = \varepsilon_{0\nu\beta\beta}\frac{a_i N_A}{W}\Gamma_{0\nu}, \quad (9)$$

where $\varepsilon_{0\nu\beta\beta}$ is the total signal efficiency calculated in Sec. IV, a_i is the isotopic abundance of ^{130}Te, 34.167%, W is the molar mass of TeO_2 and N_A is Avogadro's number.

The resulting best-fit parameters are listed in Table II and the best-fit model is shown in Fig. 10.

TABLE II. The best-fit parameters from the ROI fit. The ^{60}Co peak position, E^{Co}, is constructed from the fit parameter Δ as $E^{\mathrm{Co}} = 2614.511 - \Delta$.

$R^{\mathrm{Co}}(0)$	0.92 ± 0.24 counts/(kg yr)
E^{Co}	2507.6 ± 0.7 keV
b_{ROI}	0.058 ± 0.004 counts/(keV kg yr)
$\Gamma_{0\nu}$	$0.01 \pm 0.12 \times 10^{-24}$ yr^{-1}

1. Consistency of model

We perform several goodness-of-fit tests of the model. We measure a χ^2 from the binned data in Fig. 10 of 43.9 for 46 degrees of freedom. In a large set of pseudoexperiments generated from the best-fit model, we find that about 90% of experiments return a larger χ^2. We find similar consistency according to both Kolmogorov-Smirnov and Anderson-Darling metrics [35].

We also postulate an extra signal peak at the most significant positive fluctuation around 2535 keV, but with the position left unconstrained. This returns an improvement in the fit of $\Delta\chi^2 = 4.72$. The probability of such a fluctuation occurring by chance is 3% for 1 extra degree of freedom; however the probability of it occurring by chance anywhere in the 100 keV ROI (i.e., the "look-elsewhere effect") is ≈40%, so we are unable to conclude that the fluctuation is physical. For comparison, fitting the spectrum without a line for ^{60}Co yields a $\Delta\chi^2 = 24.3$ for 2 degrees of freedom. Thus the probability of this peak occurring by chance is 0.0005%.

D. Systematics accounting

The primary sources of systematic uncertainty are listed in Table III. We consider two types of systematic uncertainties: a systematic scaling $\sigma_{\mathrm{scaling}}$ which contributes an uncertainty

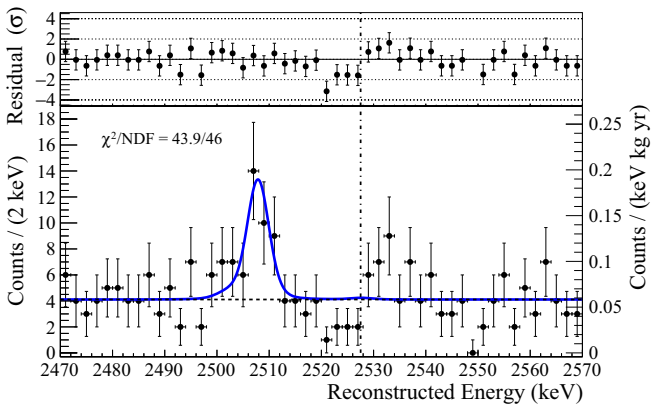

FIG. 10. Bottom panel: The best-fit model (solid blue lines) overlaid on the CUORE-0 energy spectrum (*data points*). For simplicity, the data are shown with Gaussian error bars. The peak at 2507 keV is due to ^{60}Co and the dash-dotted line indicates the position at which we expect a potential $0\nu\beta\beta$ decay signal. The dashed black line indicates the continuum background component in the ROI. Top panel: The normalized residuals of the best fit model and the binned data points. Figure from [11].

TABLE III. Summary of the systematic uncertainties and their effect on the $0\nu\beta\beta$ decay rate. Adapted from [11].

	Additive (10^{-24} yr^{-1})	Scaling (%)
Signal detection	–	0.7
Energy resolution	0.006	2.6
Energy scale	0.006	0.4
Bkg function	0.004	0.7
Lineshape	0.004	1.3
Fit bias	0.006	0.15

proportional to the true decay rate, and an additive systematic uncertainty σ_{add} which is independent of the decay rate. The effect of the uncertainty on the signal detection efficiency $\varepsilon_{0\nu\beta\beta}$ is a straightforward scaling uncertainty. We estimate the effect of the other uncertainties on the measured decay rate using a large ensemble of pseudoexperiments.

For the uncertainty on the energy resolution scaling α_σ and the uncertainty on the energy scale $\Delta\mu(Q_{\beta\beta})$ we modify the parameter value by 1σ, redo the fit, and generate a set of Monte Carlo spectra with the new best fit parameters and a simulated $0\nu\beta\beta$ decay rate ranging from 0–2×10^{-24} yr. For each generated spectrum, the number of events is Poisson distributed with the expected number of events for that set of parameters and signal. We fit the Monte Carlo spectra with the unmodified parameters and regress the resulting measured decay rates against the simulated values to determine σ_{add} and $\sigma_{\mathrm{scaling}}$ for each systematic uncertainty.

We perform a similar procedure for the choice of background model and detector response lineshape. For the former, we simulate spectra using best-fit background model with either a first or second-degree polynomial and determine the effect on the measured decay rate. For the lineshape, we simulate data with a single Gaussian lineshape (i.e., with $\eta_i = 0$).

Finally, we also take into account any potential bias introduced from the fitting procedure itself. We calculate this bias in the same way described above, but with no parameters modified and the number of events fixed to 233. The results for the considered sources of systematic errors are summarized in Table III.

Including systematics, our best-fit $0\nu\beta\beta$ decay rate is

$$\hat{\Gamma}_{0\nu} = [0.01 \pm 0.12\,(\mathrm{stat}) \pm 0.01\,(\mathrm{syst})] \times 10^{-24}\,\mathrm{yr}^{-1}. \quad (10)$$

We follow a similar procedure to calculate the systematic error on the background rate in the ROI, b_{ROI}, and obtain

$$b_{\mathrm{ROI}} = 0.058 \pm 0.004\,(\mathrm{stat}) \pm 0.002\,(\mathrm{syst})\ \mathrm{counts/(keVkgyr)}. \quad (11)$$

Using this value, we calculate the 90% C.L. sensitivity of the experiment, as the median 90% C.L. limit of a large number of MC pseudoexperiments generated with this expected background and no $0\nu\beta\beta$ decay signal. The resulting 90% C.L. sensitivity is 2.9×10^{24} yr—slightly surpassing the Cuoricino sensitivity and limit [CINO2011].

E. Limit evaluation

Since our best fit value of $\Gamma_{0\nu}$ is compatible with 0, we conclude that we see no evidence of a $0\nu\beta\beta$ decay signal and set a Bayesian upper limit on the $0\nu\beta\beta$ decay rate of ^{130}Te. We eliminate our nuisance parameters $\nu \equiv \{R^{\mathrm{Co}}(0), E^{\mathrm{Co}}, b_{\mathrm{ROI}}\}$ by maximizing the likelihood over them and calculating the likelihood ratio, $\mathcal{L}_{\mathrm{PR}}$:

$$\mathcal{L}_{\mathrm{PR}}(\Gamma_{0\nu}) \equiv \frac{\mathcal{L}|_{\max \nu}(\Gamma_{0\nu}, \nu)}{\mathcal{L}(\hat{\Gamma}_{0\nu}, \hat{\nu})}, \tag{12}$$

where $\hat{\Gamma}_{0\nu}$, $\hat{\nu}$ are the best-fit values.

We evaluate our upper limit Γ_{Limit} at a confidence of α_{CL} as

$$\alpha_{\mathrm{CL}} = \frac{\int_{-\infty}^{\Gamma_{\mathrm{Limit}}} \mathcal{L}_{\mathrm{PR}}(\Gamma)\pi(\Gamma)\,\mathrm{d}\Gamma}{\int_{-\infty}^{\infty} \mathcal{L}_{\mathrm{PR}}(\Gamma)\pi(\Gamma)\,\mathrm{d}\Gamma}, \tag{13}$$

where $\pi(\Gamma)$ is the prior on $\Gamma_{0\nu}$. We assume a flat prior in the physical region, $\pi(\Gamma) = 1$ for $\Gamma \geqslant 0$ and $\pi(\Gamma) = 0$ otherwise.

We place an upper limit of $\Gamma_{0\nu} < 0.25 \times 10^{-24}$ yr^{-1} or $T^{0\nu}_{1/2} > 2.7 \times 10^{24}$ yr at 90% C.L (only accounting for statistical uncertainties) [11]. This limit is slightly worse than our median expected 90% C.L. sensitivity of 2.9×10^{24} yr due to a slight upward fluctuation at $Q_{\beta\beta}$. The probability to obtain a more stringent limit is 55%.

We account for our systematic uncertainties by first combining them in quadrature to create a single $\sigma_{\mathrm{syst}}(\Gamma)$:

$$\sigma^2_{\mathrm{syst}}(\Gamma) \equiv \sum_i \sigma^2_{\mathrm{add},i} + \sigma^2_{\mathrm{scaling},i}\Gamma^2, \tag{14}$$

where the sum runs over all systematic uncertainties. We include this in our profile likelihood curve, $\mathcal{L}_{\mathrm{PR}}(\Gamma)$, using the method outlined in CINO2011. We denote

$$\chi^2_{\mathrm{stat}} \equiv 2\mathrm{NLL}_{\mathrm{stat}} = -2\log \mathcal{L}_{\mathrm{PR}}. \tag{15}$$

We assume a Gaussian distribution for our total systematic uncertainty such that the measured $\Gamma_{0\nu}$ is normally distributed around the best-fit value $\hat{\Gamma}_{0\nu}$, with variance σ^2_{syst}. We construct the function $\chi^2_{\mathrm{syst}} \equiv (\Gamma_{0\nu} - \hat{\Gamma}_{0\nu})^2/\sigma^2_{\mathrm{syst}}$ and combine statistical and systematic uncertainties into a total χ^2_{tot} distribution:

$$\frac{1}{\chi^2_{\mathrm{tot}}(\Gamma)} = \frac{1}{\chi^2_{\mathrm{stat}}(\Gamma)} + \frac{1}{\chi^2_{\mathrm{syst}}(\Gamma)}. \tag{16}$$

From χ^2_{tot} we can calculate the negative-log-likelihood including systematics, $\mathrm{NLL}_{\mathrm{stat+syst}} \equiv \frac{1}{2}\chi^2_{\mathrm{tot}}$. The negative log likelihoods, $\mathrm{NLL}_{\mathrm{stat}}$ and $\mathrm{NLL}_{\mathrm{stat+syst}}$, are plotted in Fig. 14 and the difference between them is almost negligible. At our 90% limit, the systematic uncertainty only accounts for 5% of our total uncertainty, so these results are statistics limited. Including the systematic uncertainties, we set a limit on the $0\nu\beta\beta$ decay rate of ^{130}Te of $\Gamma_{0\nu} < 0.25 \times 10^{-24}$ yr^{-1} or $T^{0\nu}_{1/2} > 2.7 \times 10^{24}$ yr at 90% C.L. [11].

VII. DISCUSSION OF FIT RESULTS AND DETECTOR PERFORMANCE

A. Detector energy resolution

To characterize the energy resolution of our detector, we quote the FWHM at the ^{208}Tl energy in calibration runs. Each BoDs has its own best fit probability density function (PDF), for which we numerically evaluate the FWHM. We measure the FWHM of the summed primary and secondary peaks without the background continuum. This yields a distribution of FWHM values, one for each BoDs, which is shown in Fig. 11.

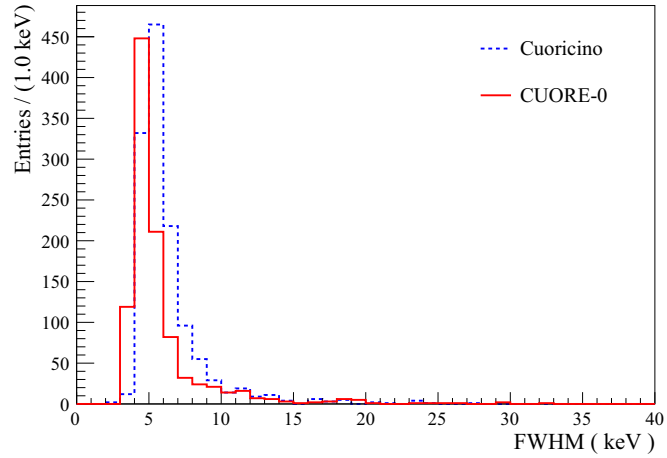

FIG. 11. The distribution of FWHM values for each BoDs for CUORE-0 (red–solid lines) compared to the similar distribution for Cuoricino (blue–dashed lines).

In order to quote a single FWHM value characteristic of the entire detector performance, we calculate an effective FWHM which is obtained by averaging detector sensitivities (i.e., we quote the resolution of a single bolometer with equivalent sensitivity). Numerically, this is a weighted harmonic mean of resolutions:

$$\text{Effective FWHM} = \sum_i T_i \Big/ \sum_i \frac{T_i}{\Delta E_i}, \tag{17}$$

where T_i is the physics exposure of bolometer-dataset i. For convenience, we also quote the combined FWHM values, which are defined as the FWHM of the combined PDF fits to the calibration data shown in Fig. 8(b). The resulting resolution values are shown in Table IV. We also quote the projected resolution at $Q_{\beta\beta}$ in the physics spectrum, 5.1 ± 0.3 keV, by multiplying the effective FWHM for the full CUORE-0 data by $\alpha_\sigma(Q_{\beta\beta})$.

TABLE IV. FWHM values for CUORE-0 and Cuoricino data measured on the calibration ^{208}Tl 2615 keV line (see text for details).

	Combined FWHM (keV)	Effective FWHM (keV)
CUORE-0 Campaign I	5.3	5.7
CUORE-0 Campaign II	4.6	4.8
CUORE-0 Total	4.8	4.9
Cuoricino		5.8

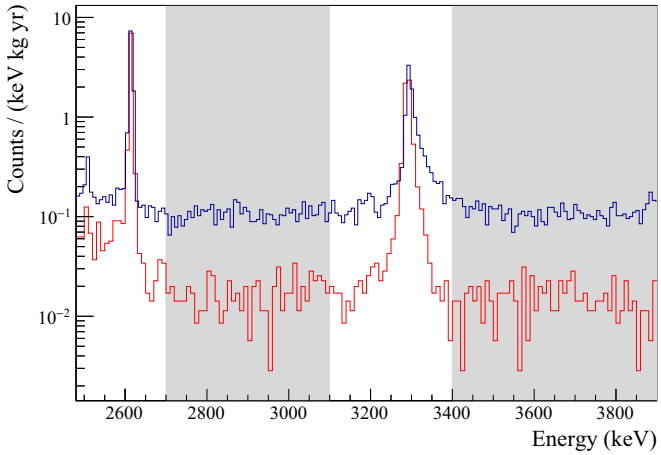

FIG. 12. The α-continuum region for CUORE-0 (red lower line) and Cuoricino (blue upper line). The regions over which the α continuum is evaluated are the shaded regions from 2700–3900 excluding the ^{190}Pt peak. Note that the ^{190}Pt peak reconstructs ~40 keV too high due to the quenching of α particles in the bolometers; this is discussed further in [24].

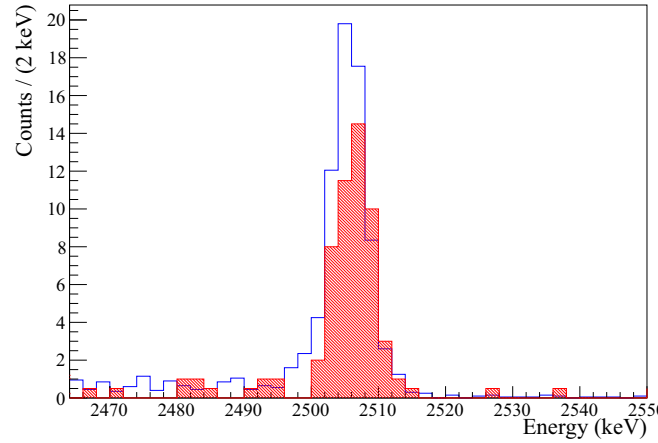

FIG. 13. The spectrum from the dedicated ^{60}Co calibration measurement. The single-crystal coincidence peak (red shaded) reconstructs 2 keV higher than the summed energy peak from the two-crystal coincidence (blue).

B. CUORE-0 background rate

In order to quantify the background reduction achieved relative to Cuoricino, and to compare with the projections for CUORE, we consider the background rate in two regions of the spectrum: the α- region and the ROI. The α- background is measured over the range 2700–3900 keV, which is dominated by degraded α decays. We exclude the range 3100–3400 keV which contains a peak from the decay of ^{190}Pt (see Fig. 12). ^{190}Pt is a naturally occurring isotope that contaminates our bolometers during the crystal growth process. However, since the contamination is usually in the form of inclusions within the crystal bulk, the α particles emitted in these decays do not degrade and thus do not contribute to the background in the ROI. We also see no evidence for a ^{190}Pt peak in the two-crystal coincidence spectrum, which indicates that the contamination is not near the surface [24]. Over the α-continuum range, we measure an average rate of $b_\alpha = 0.016 \pm 0.001$ counts/(keV kg yr). This is in agreement with our projected background for CUORE-0. Comparing this to the value measured in Cuoricino, $b_\alpha = 0.110 \pm 0.001$ counts/(keV kg yr), we see an improvement of a factor of 6.8.

The background in the ROI is expected to have both an α component which extends down from the α region discussed above and a γ component from ^{208}Tl 2615 keV γ rays which undergo low angle scattering before being absorbed in a bolometer or multiple scattering in a single bolometer before escaping. We measure the background rate in the ROI from the UEML fit to the ROI, $b_{\mathrm{ROI}} = 0.058 \pm 0.004$ counts/(keV kg yr). This is an improvement of a factor of 2.7 over Cuoricino, which obtained $b_{\mathrm{ROI}} = 0.153 \pm 0.006$ counts/(keV kg yr) in its similarly sized unenriched crystals [CINO2011]. Taking the difference between b_{ROI} and b_α, we can estimate the γ background component to be $b_\gamma = 0.042 \pm 0.004$ counts/(keV kg yr) and $b_\gamma = 0.043 \pm 0.006$ counts/(keV kg yr) for CUORE-0 and Cuoricino, respectively. This is consistent with our models that place the origin of the γ contamination in the cryostat materials, which are common to both CUORE-0 and Cuoricino [24]. This γ background forms an irreducible background for CUORE-0, but is expected to be significantly reduced in CUORE due to better material selection, better shielding, and more efficient anticoincidence rejection.

Overall, CUORE-0 successfully validated the background reduction measures developed for CUORE and we believe that the CUORE background goal of $b_{\mathrm{ROI}} = 0.01$ counts/(keV kg yr) is within reach. A projection of the CUORE-0 results to the CUORE background will be detailed in a paper currently in preparation [24].

C. Position of the ^{60}Co sum peak

In Table II, we observe that the single-crystal ^{60}Co coincidence peak reconstructs 1.9 ± 0.7 keV higher than expected. A similar effect was seen in Cuoricino, where the peak reconstructed too high by 0.8 ± 0.3 keV (using a different lineshape and fitting procedure). In CINO2011, we took this shift as a systematic uncertainty on our $0\nu\beta\beta$ peak position; however, in Fig. 9(a) this peak is a clear outlier. We confirmed this effect with a dedicated calibration measurement with ^{60}Co sources. The total energy from a two-crystal coincidence—when the two γ rays are absorbed in two distinct crystals—reconstructs at the expected energy whereas the single-crystal coincidence reconstructs too high by 2 keV, see Fig. 13.

At present, we are still investigating the cause of this effect, but we hypothesize that it is due to a difference in the geometric spread in the energy deposition in the crystal. A coincidence of two γ rays in a single crystal can spread the energy over a larger volume of the bolometer, and this may affect the bolometric gain. The difference in energy deposition topologies is borne out in MC simulations, however the mechanism connecting this to the gain is still uncertain. This hypothesis is supported by the fact that the single-escape peak from ^{208}Tl at 2104 keV

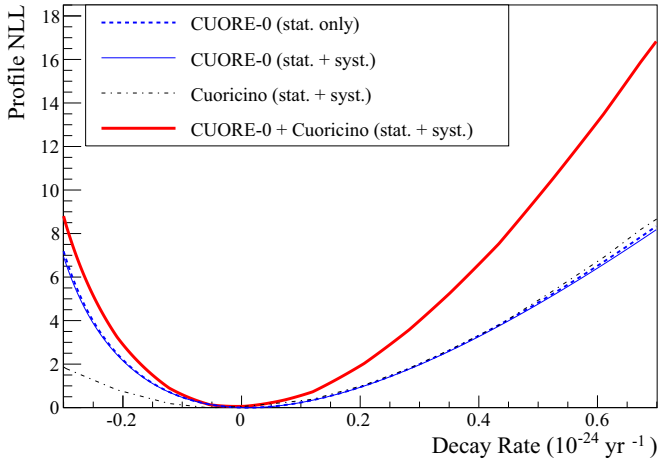

FIG. 14. Combined negative log-likelihood (NLL) curves for CUORE-0, Cuoricino, and their combined curves. Figure from [11].

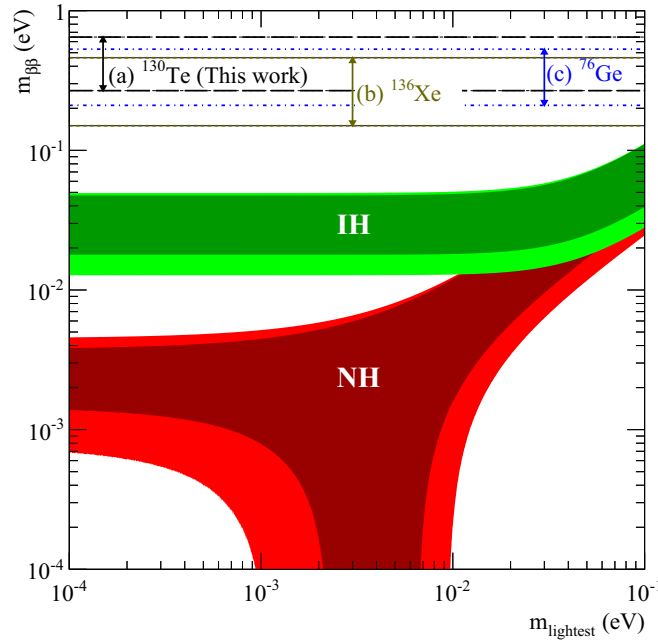

FIG. 15. Plot of the allowed regions for $m_{\beta\beta}$ as a function of the lightest neutrino mass, m_{lightest}, assuming the light Majorana neutrino exchange model of $0\nu\beta\beta$ decay. The exclusion bands represent 90% C.L., with the vertical width coming from the uncertainty in the NME. The exclusion from ^{76}Ge is from [8]. The exclusion from ^{136}Xe is the combined limits from [9,10]. The exclusion from ^{130}Te is the result of this paper. Figure from [11].

also reconstructs significantly higher than expected, by 0.84 ± 0.22 keV. This peak is caused by pair production in a crystal, followed by an annihilation to two 511 keV γ rays, one of which is reabsorbed in the same crystal. The double escape peak in the physics data at 1593 keV reconstructs within 0.13 ± 0.30 keV of the expected value, following the trend of the other peaks in the physics spectrum. We conclude from this that these events, and consequently the $0\nu\beta\beta$ decay events which are topologically similar, are not shifted by the same effect as the ^{60}Co single crystal coincidence. We note however, that in the calibration spectrum, this peak reconstructs low by -0.66 ± 0.02 keV. We continue to investigate the origin of this discrepancy.

VIII. COMBINATION WITH Cuoricino

In this section we combine the results of CUORE-0 with those of Cuoricino (19.75 kg yr of ^{130}Te). The Cuoricino experimental design and data analysis has already been addressed in this document and the details and final $0\nu\beta\beta$ decay results can be found in CINO2011.

We combine the CUORE-0 likelihood curve with the one from Cuoricino[1] (see Fig. 14) and set a combined limit on the $0\nu\beta\beta$ decay rate of ^{130}Te at $\Gamma_{0\nu} < 0.17 \times 10^{-24}$ yr^{-1} or $T^{0\nu}_{1/2} > 4.0 \times 10^{24}$ yr at 90% C.L. [11].

In addition to our Bayesian limit, we also report a frequentist limit using the Rolke technique [36]. For CUORE-0 we obtain $T^{0\nu}_{1/2} > 2.8 \times 10^{24}$ yr including systematic uncertainties and $T^{0\nu}_{1/2} > 4.1 \times 10^{24}$ yr for the combined bolometric limit.

We interpret our combined Bayesian half-life limit in the context of $0\nu\beta\beta$ decay mediated by the exchange of light Majorana neutrinos [37] and place a limit on the effective Majorana mass, $m_{\beta\beta}$, where $m_{\beta\beta}$ is defined by

$$\frac{1}{T^{0\nu}_{1/2}} = G_{0\nu}|\mathcal{M}_{0\nu}|^2 \frac{m^2_{\beta\beta}}{m^2_e}. \tag{18}$$

Using the phase space factors $G_{0\nu}$ from [37], and assuming a value of $g_A \simeq 1.27$, we can place the following range of limits for the most recent nuclear matrix element (NME), $|\mathcal{M}_{0\nu}|^2$, calculations:

(i) $m_{\beta\beta} < 520$–650 meV for interacting shell model calculations from [38];
(ii) $m_{\beta\beta} < 300$–340 meV for the quasiparticle-random phase approximation (QRPA) calculation from [39];
(iii) $m_{\beta\beta} < 340$ meV for the QRPA calculation from [40];
(iv) $m_{\beta\beta} < 360$ meV for the interacting boson model calculation from [41];
(v) $m_{\beta\beta} < 270$ meV for the energy density functional calculations from [42];
(vi) $m_{\beta\beta} < 700$–760 meV for the shell model from [43].

Using all available calculations, we place a limit range on the effective Majorana mass of $m_{\beta\beta} < 270$–760 meV [11]. However, since the shell model calculations from [43] are not presently available for other isotopes, we present an alternative limit useful for comparison with limits from ^{76}Ge and ^{136}Xe, $m_{\beta\beta} < 270$–650 meV. This latter limit is presented in Fig. 15.

[1]We point out that for the purposes of combining the results, the Cuoricino profile likelihood curve has been updated to reflect a new measurement of the ^{130}Te isotopic abundance, which changed from $a_I = 0.3380(1)$ to $a_I = 0.341668 \pm 0.000016$ [22]; however, all Cuoricino results quoted here continue to reflect the old measurement.

IX. CONCLUSIONS

The CUORE-0 experiment ran for two years from 2013 to 2015 and collected 35.2 kg yr of TeO_2 exposure or 9.8 kg yr of ^{130}Te exposure. The improved background level of the detector allows us to reproduce the sensitivity of the Cuoricino experiment in ∼40% the time. In this paper, we fully describe the procedure adopted for the analysis of this data that was presented in [11], which placed a 90% C.L. Bayesian limit on the $0\nu\beta\beta$ decay half-life of ^{130}Te at $T^{0\nu}_{1/2} > 2.7 \times 10^{24}$ yr and a combined limit with the Cuoricino data of $T^{0\nu}_{1/2} > 4.0 \times 10^{24}$ yr. This corresponds to a limit range on the effective Majorana mass of $m_{\beta\beta} < 270$–760 meV, using the most up-to-date NME calculations.

These results also validate the techniques we have developed in preparation for CUORE. We have achieved the CUORE energy resolution goal of 5 keV FWHM at 2615 keV. We also achieved a background of $b_{\mathrm{ROI}} = 0.058 \pm 0.004$ counts/(keV kg yr) in the ROI and $b_{\alpha} = 0.016 \pm 0.001$ counts/(keV kg yr) in the α continuum, which are in line with our predictions and gives us confidence that the CUORE goal is within reach. We have developed an algorithm to improve the energy resolution by deconvolving signals from multiple bolometers, and a TGS algorithm to recover data from bolometers with missing Joule heaters. We have improved the efficiency of our anticoincidence cut, which will be necessary in the larger CUORE detector. Finally, we have implemented a data blinding technique that is both robust and effective.

This analysis has also highlighted several open issues that will be addressed for CUORE. As a result of our improved energy resolution, we saw a more complicated lineshape than previously seen. We seek to understand the source of this substructure and its effect on our expected $0\nu\beta\beta$ decay signal. We found a small energy-dependent bias in our energy reconstruction at the level of 0.1 keV that we seek to address in CUORE. Finally, we have seen a significant shift in the reconstructed energy of the single-crystal coincidence peaks, ^{60}Co and the ^{208}Tl single escape. Moving forward, we plan to investigate the sources of these effects and their impacts on our $0\nu\beta\beta$ analysis as we push to better understand our detectors.

ACKNOWLEDGMENTS

The CUORE Collaboration thanks the directors and staff of the Laboratori Nazionali del Gran Sasso and the technical staff of our laboratories. This work was supported by the Istituto Nazionale di Fisica Nucleare (INFN); the National Science Foundation under Grant Nos. NSF-PHY-0605119, NSF-PHY-0500337, NSF-PHY-0855314, NSF-PHY-0902171, NSF-PHY-0969852, NSF-PHY-1307204, NSF-PHY-1314881, NSF-PHY-1401832, and NSF-PHY-1404205; the Alfred P. Sloan Foundation; the University of Wisconsin Foundation; and Yale University. This material is also based upon work supported by the US Department of Energy (DOE) Office of Science under Contract Nos. DE-AC02-05CH11231, DE-AC52-07NA27344, and DE-SC0012654; and by the DOE Office of Science, Office of Nuclear Physics under Contract Nos. DE-FG02-08ER41551 and DE-FG03-00ER41138. This research used resources of the National Energy Research Scientific Computing Center (NERSC).

[1] W. H. Furry, Phys. Rev. **56**, 1184 (1939).
[2] F. T. Avignone III, S. R. Elliott, and J. Engel, Rev. Mod. Phys. **80**, 481 (2008).
[3] G. Feinberg and M. Goldhaber, Proc. Nat. Acad. Sci. **45**, 1301 (1959).
[4] B. Pontecorvo, Sov. Phys. JETP **26**, 984 (1968).
[5] A. Giuliani and A. Poves, Adv. High Energy Phys. **2012**, 857016 (2012).
[6] O. Cremonesi and M. Pavan, Adv. High Energy Phys. **2014**, 951432 (2014).
[7] A. Barabash, Phys. Procedia **74**, 416 (2015).
[8] M. Agostini *et al.* (GERDA Collaboration), Phys. Rev. Lett. **111**, 122503 (2013).
[9] J. Albert *et al.* (EXO-200 Collaboration), Nature **510**, 229 (2014).
[10] A. Gando *et al.* (KamLAND-Zen Collaboration), Phys. Rev. Lett. **110**, 062502 (2013).
[11] K. Alfonso *et al.* (CUORE Collaboration), Phys. Rev. Lett. **115**, 102502 (2015).
[12] C. Arnaboldi *et al.*, Nucl. Instrum. Methods Phys. Res. A **518**, 775 (2004).
[13] R. Ardito *et al.*, arXiv:hep-ex/0501010 [hep-ex].
[14] C. Arnaboldi *et al.* (Cuoricino Collaboration), Phys. Lett. B **584**, 260 (2004).
[15] C. Arnaboldi *et al.* (Cuoricino Collaboration), Phys. Rev. C **78**, 035502 (2008).
[16] E. Andreotti *et al.* (Cuoricino Collaboration), Astropart. Phys **34**, 822 (2011).
[17] F. Alessandria *et al.* (CUORE Collaboration), Astropart. Phys **45**, 13 (2013).
[18] C. Arnaboldi *et al.*, J. Cryst. Growth **312**, 2999 (2010).
[19] F. Alessandria *et al.* (CUORE Collaboration), Astropart. Phys. **35**, 839 (2012).
[20] C. Arduino *et al.* (CUORE Collaboration), arXiv:1604.05465 [physics.ins-det] [J. Instrum. (to be published)].
[21] D. R. Artusa *et al.* (CUORE Collaboration), Eur. Phys. J. C **74**, 2956 (2014).
[22] M. A. Fehr, M. Rehkämper, and A. N. Halliday, Int. J. Mass Spectrom. **232**, 83 (2004).
[23] M. Redshaw, B. J. Mount, E. G Myers, and F. T. Avignone, Phys. Rev. Lett. **102**, 212502 (2009).
[24] C. Alduino *et al.* (CUORE Collaboration), (2016) (unpublished).
[25] E. E. Haller *et al.*, in *Neutron Transmutation Doping of Semiconductor Materials*, edited by R. D. Larrabee (Springer, New York, 1984).
[26] E. Fiorini and T. Niinikoski, Nucl. Instrum. Methods Phys. Res. A **224**, 83 (1984).
[27] C. Enss and D. McCammon, J. Low Temp. Phys. **151**, 5 (2008).
[28] E. Gatti and P. Manfredi, La Rivista del Nuovo Cimento **9**, 1 (1986).
[29] C. Mancini-Terracciano and M. Vignati, J. Instrum. **7**, P06013 (2012).

[30] J. Ouellet, Ph.D. thesis, University of California, Berkeley (2015).
[31] A. Alessandrello *et al.*, Nucl. Instrum. Methods Phys. Res. A **412**, 454 (1998).
[32] S. Agostinelli *et al.*, Nucl. Instrum. Methods Phys. Res. A **506**, 250 (2003).
[33] B. S. Wang, E. B. Norman, N. D. Scielzo, A. R. Smith, K. J. Thomas, and S. A. Wender, Phys. Rev. C **92**, 024620 (2015).
[34] W. Verkerke and D. Kirkby, arXiv:physics/0306116 [physics.data-an].
[35] T. W. Anderson and D. A. Darling, Ann. Math. Statist. **23**, 193 (1952).
[36] W. A. Rolke, A. M. López, and J. Conrad, Nucl. Instrum. Methods Phys. Res. A **551**, 493 (2005).
[37] J. Kotila and F. Iachello, Phys. Rev. C **85**, 034316 (2012).
[38] J. Menendez *et al.*, Nucl. Phys. A **818**, 139 (2009).
[39] F. Ŝimkovic, V. Rodin, A. Faessler, and P. Vogel, Phys. Rev. C **87**, 045501 (2013).
[40] J. Hyvarinen and J. Suhonen, Phys. Rev. C **91**, 024613 (2015).
[41] J. Barea, J. Kotila, and F. Iachello, Phys. Rev. C **91**, 034304 (2015).
[42] T. R. Rodriguez and G. Martinez-Pinedo, Phys. Rev. Lett. **105**, 252503 (2010).
[43] A. Neacsu and M. Horoi, Phys. Rev. C **91**, 024309 (2015).